PAPER • OPEN ACCESS

Coordination multi-band absorbers with patterned irrelevant graphene patches based on multi-layer film structures

View the article online for updates and enhancements.

...

Coordination multi-band absorbers with patterned irrelevant graphene patches based on multi-layer film structures

Zhiyu Bao[1]**, Jicheng Wang**[1,2,*] **, Zheng-Da Hu**[1] **, Yifan Chen**[1]**, Chengliang Zhang**[1] **and Feng Zhang**[3,*]

[1] School of Science, Jiangnan University, Wuxi 214122, People's Republic of China
[2] State Key Laboratory of Applied Optics, Changchun Institute of Optics, Fine Mechanics and Physics, Chinese Academy of Sciences, Changchun 130033, People's Republic of China
[3] Department of Physics, Xiamen University, Xiamen 361005, People's Republic of China

E-mail: jcwang@jiangnan.edu.cn and fzhang@xmu.edu.cn

Abstract
In this paper, we propose a novel absorber that combines a multi-layer film structure with graphene. The proposed structure is delicately simulated using a commercial finite element method. We combine an equivalent circuit model with parameter inversion to achieve a new method of analyzing the physical mechanism of selective absorption. The results show that four gradually decreasing peaks of ultra-high absorption are formed within 0–1.1 THz, and the maximum absorptance is near 100%. Numerical simulation and theoretical calculation are in good agreement. Due to the symmetry of the structure and the locality of surface plasmon resonance, the proposed structure is insensitive to the incident angle and the polarization state of incident light. By changing the Fermi level of the graphene, the coordination of the device is realized. By changing the height of the dielectric material to change the resonance frequency, the working frequency band is increased from 0–1.1 THz to 0–1.9 THz, and the four absorption peaks become three, which are used as sensor applications. The sensitivity of the sensors is 50 GHz RIU^{-1}, the coefficient of the determination value (R^2) obtained by linear fitting is 0.9989, and the value of the limit of detection is 5.9×10^{-5} RIU. The results show that our proposed devices have great potential in the practical application of terahertz technology absorbers and refractive index sensors.

Keywords: metamaterials, graphene-based, multi-band absorption, refractive index sensor, parameter inversion method

(Some figures may appear in color only in the online journal)

1. Introduction

Surface plasmon polaritons (SPPs) are non-radiative electromagnetic (EM) waves that are generated by the interaction of incident photons and free electrons on a metal surface's and propagate along the interface between the metal and the medium [1]. They decay exponentially in the vertical direction of the interface between the metal and the medium [2, 3]. In 1998, Ebbesen *et al* [4] found that enhanced light transmission occurs when incident light passes through the etched holes or hole arrays. This phenomenon, caused by surface plasmon resonance (SPR), breaks the diffraction limit and can control sub-wavelength light to propagate on the surface of the material. Metamaterials are artificially structured materials that can have negative permittivity and/or

permeability, which can be achieved through periodic metal-dielectric arrays or multi-layer film structures [5–9]. By arranging and combining the structural units of metamaterials, an ultra-thin two-dimensional array is formed, which we call a metasurface. It can flexibly manipulate the phase, polarization, propagation mode, and other characteristics of EM waves. Therefore, it can realize novel functions that are difficult to achieve with traditional materials, such as negative refraction [10], perfect absorption [11], and metalenses [12, 13].

As a new type of two-dimensional metamaterial, graphene has optical properties similar to metals [14–18]. The SPPs in graphene interact with the photons of the incident light through the collective resonance of surface electrons, so that the electric and magnetic fields of the incident light can be better localized on the surface of the material, thereby enhancing the absorption of incident light [19–22]. Therefore, the use of this interaction between graphene SPPs and optical matter can produce many applications, including plasma-based graphene modulators [23–28] and sensors [29–32].

A device designed as an absorber is realized by a periodic metal-dielectric array that uses the strong interaction between the planar metal element array and the incident light to enhance the absorption of EM fields [33–36]. When the incident light is in contact with the surface metal resonant element array, these SPP-based metasurface absorbers [37–41] have a common problem; that is, they have a smaller absorption spectrum. This greatly limits their application in sensing and imaging equipment. Besides, the resonance frequency of these absorbers is closely related to the shape and parameters of the patterned metal element. Therefore, we can use the two-dimensional material graphene instead of metal and combine it with the multi-layer film structure to achieve a multi-spectral absorber independent of the pattern structure. Graphene-based multiple resonance excitation will form high-order plasmon modes, forming multiple channels and dispersion of multiple plasmon resonances [42–45]. Compared with single-spectrum absorbers, a graphene-based multi-spectral absorber has better tunability and can also reduce the interference of the environment on detection accuracy.

In this article, we propose a novel absorber that has the characteristics of multi-band absorption and insensitivity to the incident angle. The absorber is based on a periodic stack of graphene and two dielectric materials. We use gold as a ground plane to reflect EM waves. On top of the gold are five periodic stacks composed of Si and polydimethylsiloxane (PDMS). The uppermost PDMS layer is between a monolayer of graphene and a patterned graphene layer. We simulate the proposed structures using the commercial finite element method (FEM) solver COMSOL Multiphysics. We use an equivalent circuit model (ECM) and parameter inversion to analyze the physical mechanism of selective absorption. Four gradually decreasing absorption peaks within 0–1.1 THz are obtained, and the maximum absorptance is almost 100%. The ECM and parameter inversion perfectly explain the reason for the four absorption peaks. Due to the high symmetry of the structure and the locality of the SPR, our proposed structures are insensitive to the incident angle and the polarization direction. In order to obtain greater sensitivity, the structural

parameters are changed to obtain three gradually decreasing absorption peaks within 0–1.9 THz, in which case the absorptance of the smallest absorption peak is 90%, and the sensor sensitivity at this time is 50 GHz RIU^{-1}. Using linear fitting to estimate the linear approximation of the frequency shift, we get $R^2 = 0.9989$. The limit of detection (LOD) of the sensor is 5.9×10^{-5} RIU.

2. Structure and theoretical analysis

A three-dimensional diagram of the proposed structure is shown in figure 1(a), where the red arrow is the incident TE wave, and the incident plane is *X–Z*. The red cuboid, yellow cuboid, and blue cuboid are gold, Si, and PDMS with thicknesses of d_{Au}, d_{Si}, and d_{PDMS}, respectively. The two black parts represent single-layer graphene and single-layer patterned graphene, respectively. The air thickness of the cover layer is denoted as d_{cover}. Within the working frequency of this article, the refractive index of PDMS [46] can be set to 1.4. The relative permittivity of the gold [47] and Si [45] can be described by the Drude model:

$$\varepsilon(\omega) = \varepsilon_\infty - \frac{\varepsilon_p}{\omega^2 + i\omega\gamma}, \tag{1}$$

where ω_∞, ε_p, and γ are the permittivity at infinite frequency, plasma frequency, and collision frequency representing loss, respectively. These values for gold and Si are 1, 1.38×10^{16} rad s^{-1} and 1.23×10^{13} s^{-1}, and 11.7, 4.94×10^{13} rad s^{-1} and 1.177×10^{13} s^{-1}, respectively. In addition, ω is the incident light angular frequency. Periodic boundary conditions in the *x* and *y* directions are set and the unit period is *P*. The widths of the upper graphene are w_1 and w_2, respectively. We have the following absorber structure parameters: $P = 100$ μm, $d_{Au} = 0.5$ μm, $d_{Si} = 22$ μm, $d_{PDMS} = 22$ μm, $d_{cover} = 5$ μm, $w_1 = 25$ μm, and $w_2 = 10$ μm.

The surface current density is utilized to simulate the monolayer graphene in the COMSOL simulation because of the smaller thickness of the monolayer graphene. We use the Kubo formula to describe the surface conductivity of the graphene layers [48–50]:

$$\sigma_{gra} = \sigma_{inter} + \sigma_{intra} = \frac{2e^2 k_B T}{\pi \hbar^2} \frac{i}{\omega + i/\tau} \ln\left[2\cosh\left(\frac{E_f}{2k_B T}\right)\right]$$
$$+ \frac{e^2}{4\hbar^2} \left[\frac{1}{2} + \frac{1}{\pi}\arctan\left(\frac{\hbar\omega - 2E_f}{2k_B T}\right)\right.$$
$$\left. - \frac{i}{2\pi} \ln\frac{(\hbar\omega + 2E_f)^2}{(\hbar\omega - 2E_f)^2 + 4(k_B T)^2}\right], \tag{2}$$

where σ_{inter} and σ_{intra} are expressed as the interband and intraband transition contributions, respectively. k_B, $\hbar$, and e represent the Boltzmann constant, reduced Plank constant, and electron charge, respectively. ω is the angular frequency of the incident radiation, E_f is the graphene Fermi energy level set to 0.2 eV, τ is the electron–phonon relaxation time set to 0.1 ps, and *T* is the ambient temperature. As we only consider highly
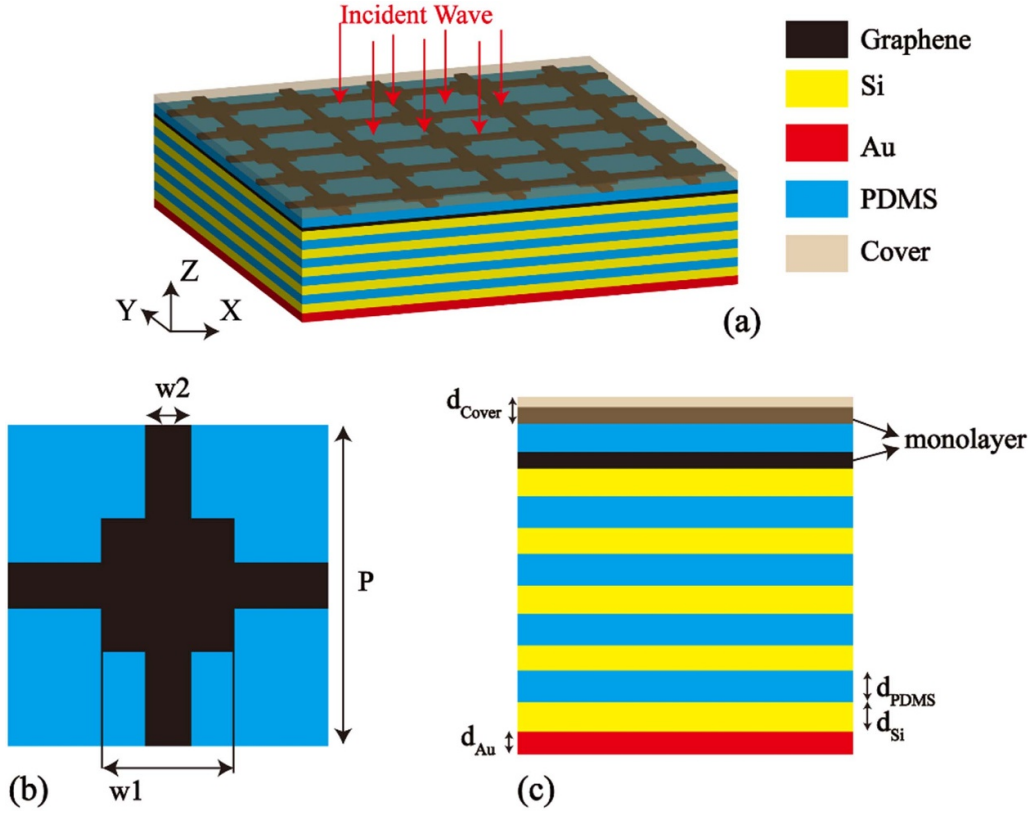
Figure 1. (a) Three-dimensional diagram of the proposed structure; (b) top view; and (c) side view.

doped graphene, we should take into account that $E_f \gg k_B T$ and $E_f \gg \hbar\omega$. Therefore, the Kubo equation can be simplified to a Drude-like equation [51, 52]:

$$\sigma_{\mathrm{gra}} = \frac{e^2 E_f}{\pi \hbar^2} \frac{i}{(\omega + i/\tau)}. \tag{3}$$

Then we use a combination of ECM and parameter inversion methods to explain the physical mechanism of the proposed structure, as shown in figure 2. Figure 2(a) is the ECM of the proposed structure. In the whole structure, the impedances of gold, Si, and PDMS are denoted as Z_{Au}, Z_{Si}, and Z_{PDMS}, respectively. The graphene plate and patterned graphene are represented by RCL circuits, and their impedance is Z_{g1} and Z_{g2}, respectively. Because the uppermost covering layer is air at this time, its impedance is neglected. Figure 2(b) is a simplified model of the equivalent circuit. Because $S_{21} = 0$ in this structure, it can be considered that Z_{Au} is short-line. At the same time, for the convenience of formula expression, we set the equivalent impedance of the multi-layer material between the graphene plate and Au as Z_{equ}.

At this point we can get the total impedance expression [43]:

$$Z_1 = jZ_{d_{\mathrm{si}}} \cdot \tan\left(\beta_d d_{\mathrm{Si}}\right) \tag{4}$$

$$Z_2 = \frac{Z_1 \cdot Z_{\mathrm{g1}}}{Z_1 + Z_{\mathrm{g1}}} \tag{5}$$

$$Z_3 = Z_{d_{\mathrm{PDMS}}} \frac{Z_2 + jZ_{d_{\mathrm{PDMS}}} \cdot \tan\left(\beta_d d_{\mathrm{PDMS}}\right)}{Z_{d_{\mathrm{PDMS}}} + jZ_2 \cdot \tan\left(\beta_d d_{\mathrm{PDMS}}\right)} \tag{6}$$

$$Z_{\mathrm{total}} = \frac{Z_3 \cdot Z_{\mathrm{g2}}}{Z_3 + Z_{\mathrm{g2}}}, \tag{7}$$

where β_d is the propagation constant of the propagating terahertz waves in the dielectric substances, $Z_{\mathrm{dSi}} = Z_0(120\pi)/\varepsilon_{\mathrm{dSi}}$ is the impedance of silicon, and $Z_{\mathrm{dPDMS}} = Z_0/\varepsilon_{\mathrm{dPDMS}}$ is the impedance of PDMS, where Z_0 is the free space impedance.

Then we let Z_{total} be the normalized impedance of the proposed structure, and the absorber is considered to be a uniform layer with material parameters μ_1 and ε_1, as shown in figure 2(c). The upper and lower layers are air with material parameters μ_0 and ε_0. According to the EM field intensity expression [51] in the conductive medium and the boundary conditions of the EM wave on the discontinuous interface, the scattering parameters can be obtained [52]:

$$\begin{cases} S_{11} = \dfrac{\Gamma_1(1 - (\mathrm{e}^{-jk_2 d})^2)}{1 - (\Gamma_1 \mathrm{e}^{-jk_2 d})^2} \\[2mm] S_{21} = \dfrac{1 - \Gamma_1^2}{1 - (\Gamma_1 \mathrm{e}^{-jk_2 d})^2} \mathrm{e}^{-jk_2 d} \end{cases}, \tag{8}$$

where $k_2 = nk_0$ is the wave number of the equivalent medium in figures 2(c) and (d) is the height of the equivalent medium, $\Gamma_1 = (Z_{\mathrm{total}} - 1)/(Z_{\mathrm{total}} + 1)$ are the reflection coefficients between medium 1 and medium 2, and $S_{21} = 0$. According to the selection of the sign [53, 54]. As a result, we can derive:
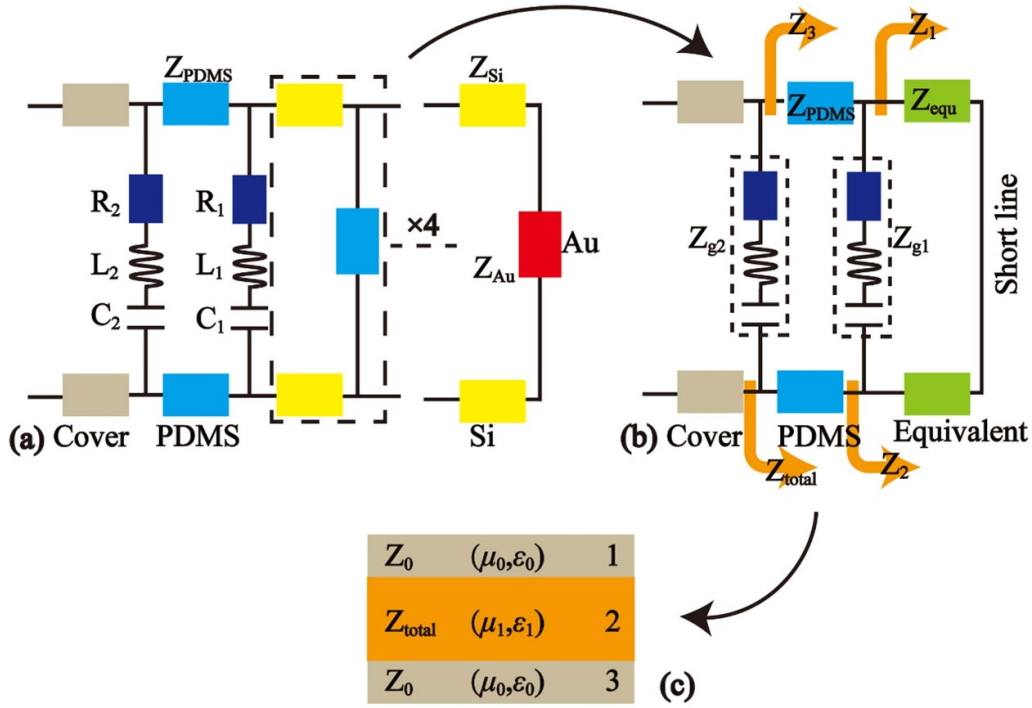
J. Phys. D: Appl. Phys. **54** (2021) 505306

Z Bao *et al*

Figure 2. (a) ECM of the proposed structure. (b) Simplified circuit model. (c) Equivalent impedance model.
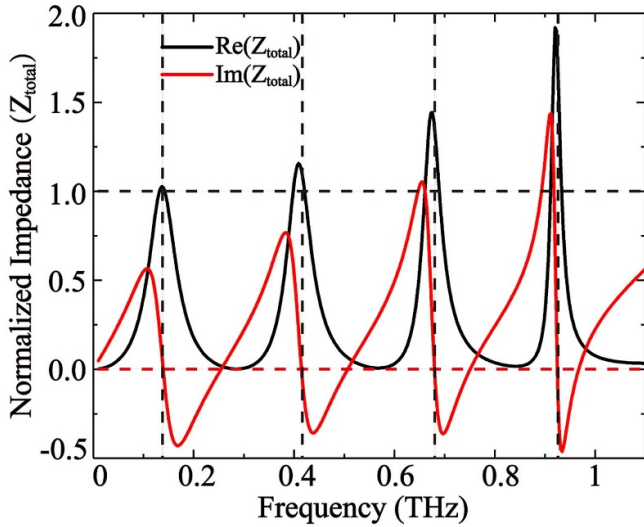

Figure 3. Normalized impedance obtained by an inversion algorithm.

$$Z_{\text{total}} = \pm \sqrt{\frac{(1+S_{11})^2 - S_{21}^2}{(1-S_{11})^2 - S_{21}^2}} = \frac{1+S_{11}}{1-S_{11}}. \qquad (9)$$

For an absorber, the closer its equivalent impedance to the free space impedance (the real part is close to one and the imaginary part is close to zero), the higher its absorptance. In figure 3, the four vertical dashed lines indicate the four resonance frequency positions. The normalized impedance obtained at the resonance frequency of 0.139 THz, 0.415 THz, 0.685 THz, and 0.931 THz are $1.0228 + 0.0019\,\text{j}$, $1.0812 + 0.0128\,\text{j}$, $1.1152 - 0.1714\,\text{j}$, and $1.1156 - 0.3587\,\text{j}$,

respectively. Therefore, it can be said that, at these four resonance frequencies, the normalized impedance of the structure is close enough to the impedance of free space, so four resonance absorption peaks appear. And as the resonance frequency increases, the difference between the four equivalent impedance values and the normalized impedance gradually becomes larger, so the absorptance of the four absorption peaks gradually decreases. This information is useful when optimizing the internal structure of the absorber as well as its composition with the purpose of minimizing reflectance and transmittance.

Figure 4 shows the absorption spectrum and reflection spectrum of the proposed structure. There are four absorption peaks in the working frequency of this absorber. The resonance frequencies are 0.139 THz, 0.415 THz, 0.685 THz, and 0.931 THz. As the frequency increases, the absorptance of the four absorption peaks gradually decreases. The first two can be considered as perfect absorption, and the absorptance of the lowest one is 95.3%. This result is also in perfect fit with the equivalent impedance we obtained earlier; that is, the closer the imaginary part of the equivalent impedance is to zero and the closer the real part is to one, the greater the absorptance.

3. Simulation results and discussion

An electric field diagram of the proposed structure at the resonance frequency is shown in figure 5. All electric field values are between 1×10^5 and $5 \times 10^5\,\text{V m}^{-1}$. From left to right, figure 5 shows the electric fields distribution at 0.139 THz, 0.415 THz, 0.685 THz, and 0.931 THz, where (a)–(d) are the top views of the electric fields, and (e)–(h) are the side views of the electric fields. It can be seen that, at 0.139 THz, the
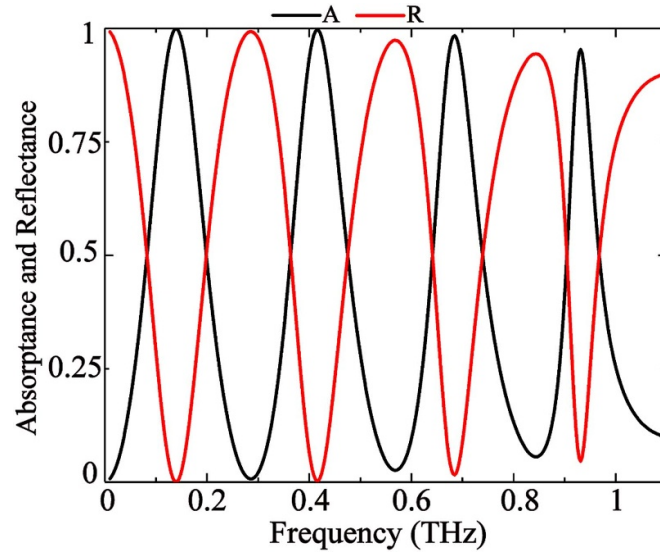
Figure 4. Absorption and reflection spectra of the proposed structure.
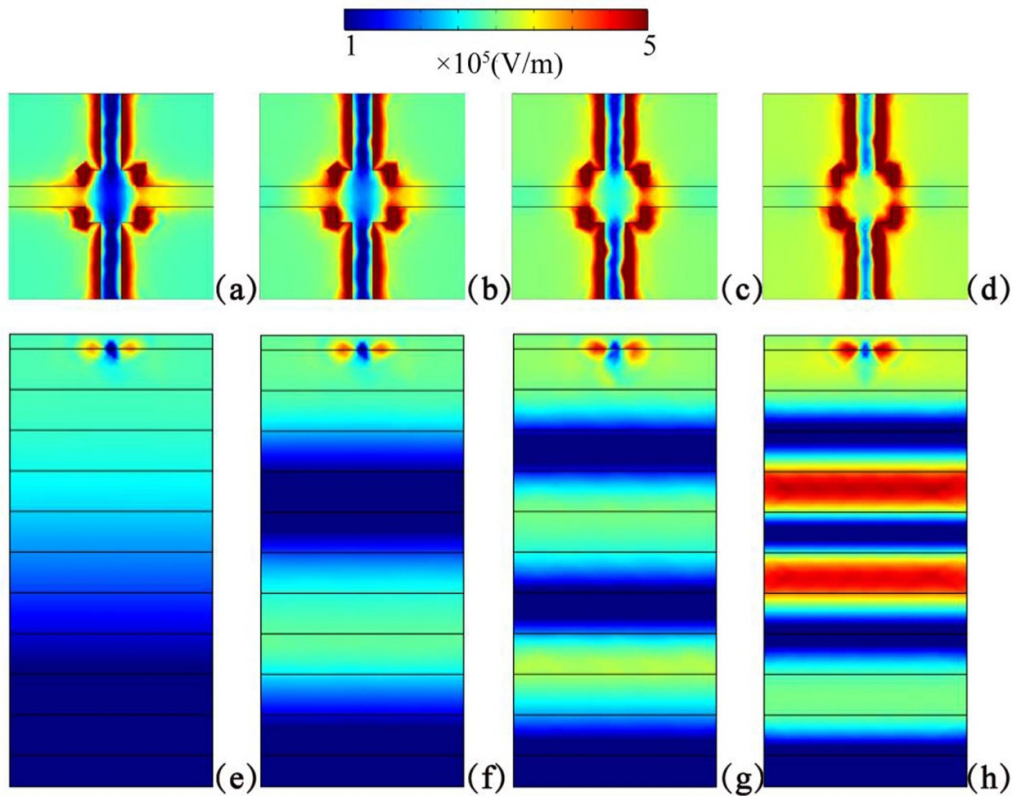

Figure 5. Electric field diagram of the proposed structure at the resonance frequency, where (a)–(d) are top views and (e)–(h) are side views.

electric field is mainly located at the edge of the patterned graphene. This is because the interaction between the patterned graphene and the incident light excites the SPR of the graphene, so a part of the electric field is localized on the edge of the patterned graphene, thereby enhancing the absorption. At the multi-layer film, the electric field gradually decreases as the incident depth increases. As the frequency increases, the local electric field of the patterned graphene layer gradually

diffuses around, and the local electric field gradually enters the multi-layer film. Not only that, the multi-layer film gradually shows the change between the high and low electric field values (figures 5(f)–(h)).

Then we change the parameters of the structure to modulate the absorptance of the absorber. As shown in figure 6(a), we change the period, *P*, of the structure, and we can see that the change in the structure period has little effect on the overall
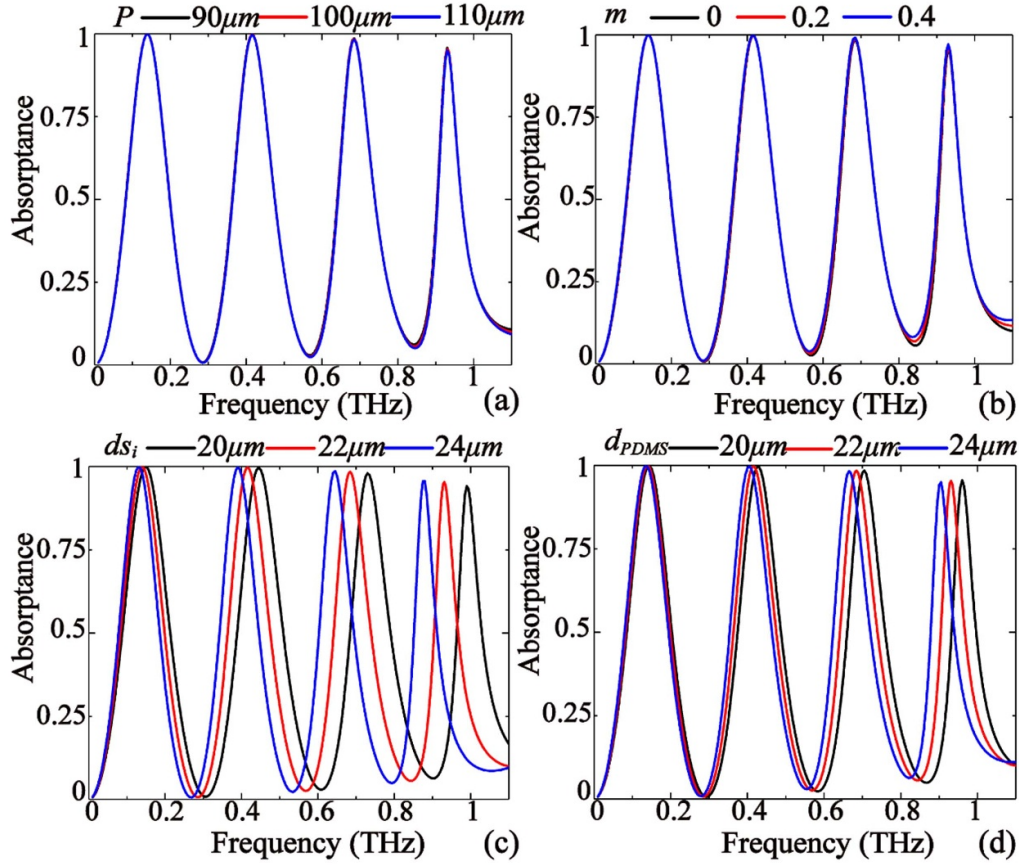
Figure 6. (a)–(d) Absorption spectra analysis with varying *P*, *m*, d_{si}, and d_{PDMS}, respectively. Other parameters are set as default. *m* is the overall magnification of the graphene parameters of the patterned graphene layer.

absorptance. Next, we magnify the overall parameters of the patterned graphene by *m* times. As shown in figure 6(b), we can see that the change of *m* has little effect on the absorption peak of the absorber. This shows that our structure does not have great requirements for the accuracy of the unit period and for the parameters of patterned graphene during the manufacturing process. Figure 6(c) shows the effect of silicon layer thickness changes on the structure absorptance (note: the thickness of each layer of silicon is the same and changes simultaneously). It can be seen that, with the increase of d_{Si}, the resonance frequency moves toward the low frequency direction, and the absorptance gradually increases. Figure 6(d) shows the influence of the thickness of the PDMS layer on the absorptance (note: the thickness of each layer of PDMS is the same and changes simultaneously). With the increase of d_{PDMS}, the resonance frequency moves in the low frequency direction, and the absorptance of each absorption peak remains basically unchanged.

From the above analysis, we can see that the two most important parameters that affect the absorption peak and absorptance of the proposed structure are d_{Si} and d_{PDMS}. *P* and *m* have little effect on the structure. Hence, we discuss the influences of the graphene plate and patterned graphene on the entire structure. In figure 7, the black curve is the absorption spectrum of the structure without the graphene layer. It can be seen that, although there are four absorption peaks
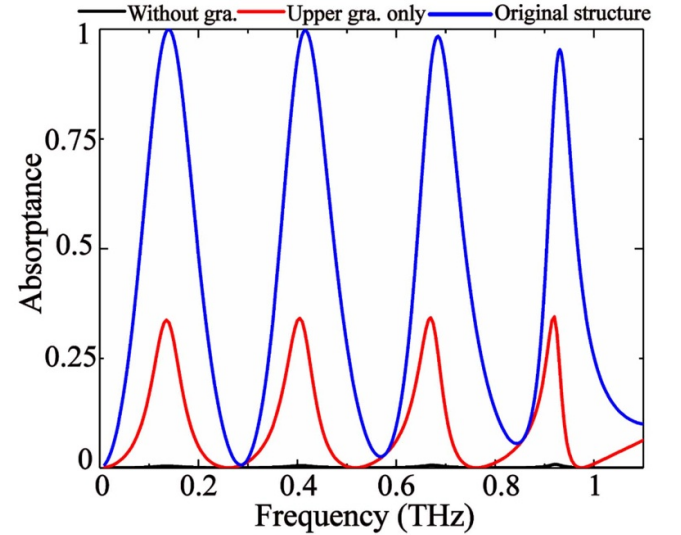

Figure 7. The influence of graphene structure on absorptance. The black curve is the structure without graphene, the red curve is the structure with only patterned graphene, and the blue curve is both patterned graphene and the graphene plate.

when there is no graphene layer, the absorptance is extremely small, which is basically close to zero. When there is only an upper layer of patterned graphene, as shown in the red curve,
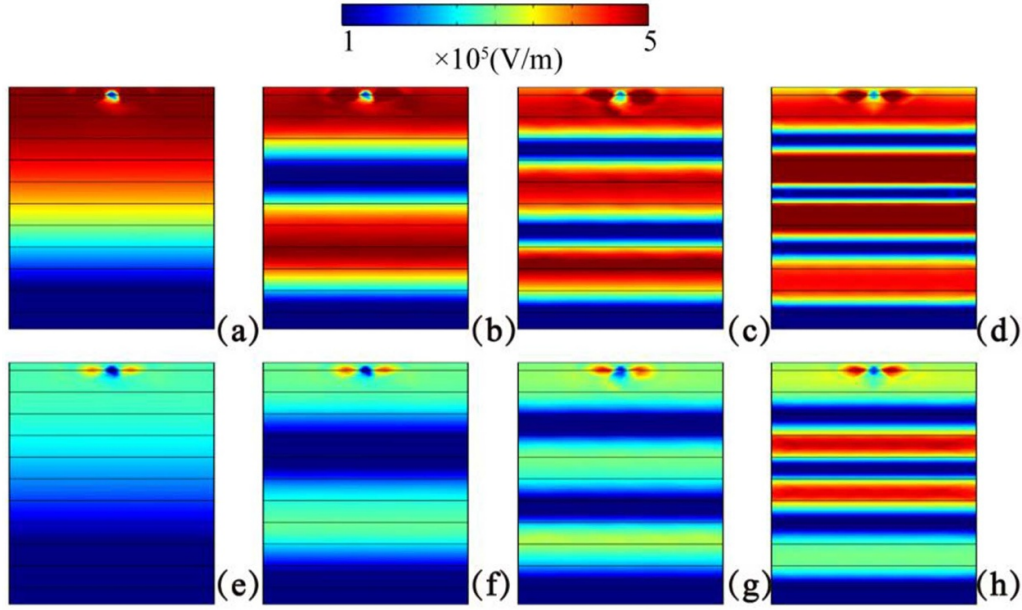
Figure 8. Comparison of electric field distribution diagrams at the resonance frequency, where (a)–(d) are only the upper layer of graphene and (e)–(h) are the original structure.

the four absorption peaks are increased, but only by about 30%. When the graphene plate is added, the smallest absorption peak among the four absorption peaks is above 95%, as shown by the blue curve. Therefore, the patterned graphene and the lower graphene mainly play a role in improving the absorptance of the overall structure.

Figures 5(a)–(d) show that the enhancement of the structure absorptance of the upper graphene is mainly reflected in the formation of local SPR. In order to study why the lower graphene enhances the structure's absorptance, we compared the side view of the electric field with and without the lower graphene, as shown in figure 8. Taking figures 8(d) and (h) as an example, it can be seen that, at the same frequency, the structure with the lower graphene can better localize the electric field between the lower graphene and the underlying metal. This is because the lower graphene, the multi-layer film structure, and the underlying gold form a symmetrical Fabry–Pérot cavity. The multiple reflections of incident light in the formed cavity enhance the absorption of incident light by the structure.

Figure 9 shows the absorption spectrum of the absorber when the Fermi level of graphene is changed. We can see that, for $E_f = 0.1$ eV, the four absorption peaks gradually decrease, and the absorptance of the largest absorption peak is less than 90%. As E_f increases to 0.2 eV, the first two absorption peaks reach perfect absorption at this time, the absorption peaks still maintain a gradual downward trend, and the minimum absorptance is greater than 95%. As E_f continues to increase, the changing trend is reversed, and the absorption peak becomes larger with the increase of the resonance frequency. At this time, the resonance frequency of the perfect absorption peak will move towards being higher. Therefore, we can select the resonance frequency for perfect absorption by changing the Fermi level of graphene.
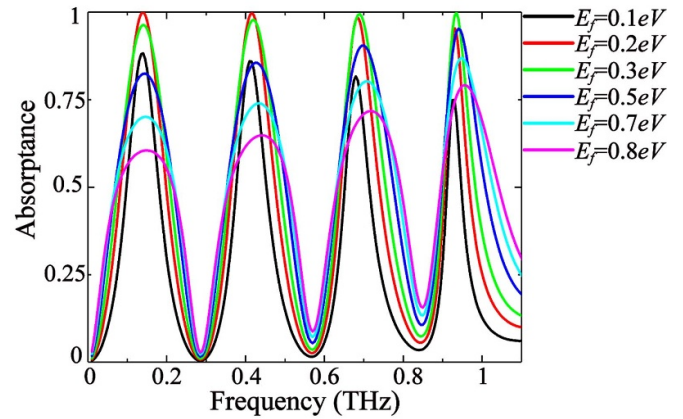

Figure 9. Absorptance as a function of the incident frequency and Fermi level.

In this article, we choose $E_f = 0.2$ eV to describe our device.

Next we explore the influences of the polarization angle and incident angle of the incident light on the absorption of the structure, as shown in figure 10. It is clear from figure 10(a) that the proposed structure is not sensitive to the polarization direction of the incident wave. This is due to the high symmetry of the proposed structure and the locality of the SPR. It can be seen from figure 10(b) that the proposed structure is not sensitive to the incident angle of the incident wave ranging from 0° to 60°. After exceeding 60°, the surface plasmon of graphene cannot be sufficiently coupled with incident photons to form SPR, resulting in a decrease in absorption.

In order to simulate the sensing application, we apply a dielectric layer on the patterned graphene. Figure 11 shows
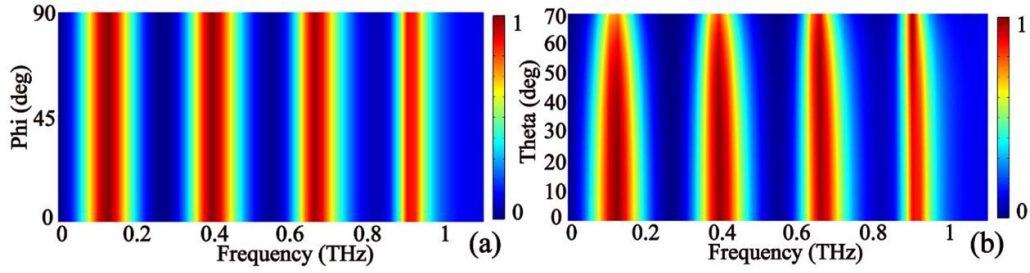
Figure 10. (a) Absorptance as a function of the incident frequency and the polarization angle. (b) Absorptance as a function of the incident frequency and the incidence angle.
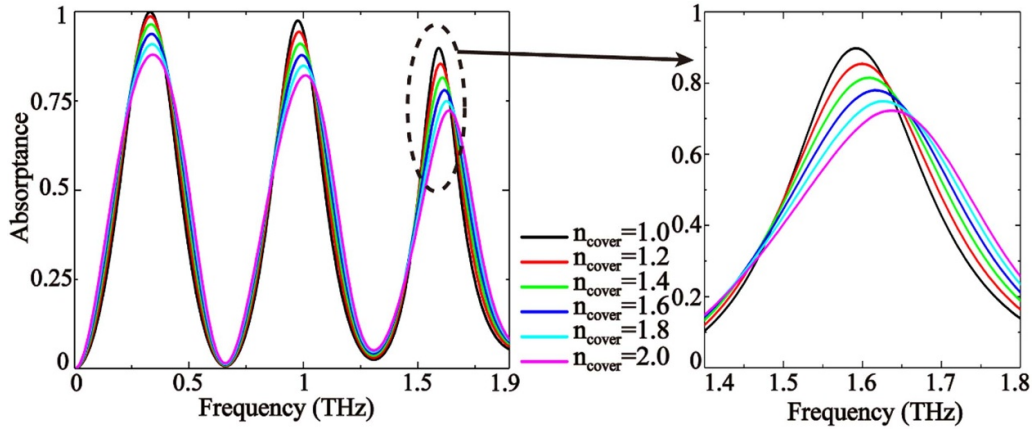

Figure 11. The absorption spectrum when the dielectric refractive index of the test object is changed. Among the changes, $d_{Si} = d_{PDMS} = 9.5$ μm, but other structural parameters remain unchanged.

the absorption characteristics of the dielectric layer with different refractive indices. In order to achieve high sensor sensitivity, we reduce d_{Si} and d_{PDMS}. At this time, $d_{Si} = 9.5$ μm, $d_{PDMS} = 9.5$ μm, and other structural parameters remain unchanged. We can see that, as the refractive index increases, the resonant frequency shifts in the high-frequency direction, thereby providing usable sensitivity. In this structure, we choose the operating frequency of the thirrd absorption peak as the operating frequency of the refractive index sensor.

We can calculate the sensitivity, *S,* of the proposed structure through the calculation formula $S = \Delta f / \Delta n$, where Δf and Δn represent the frequency shift and the change of the refractive index, respectively. In figure 12, the black solid line represents the relationship between the frequency shift and the refractive index obtained by the simulation calculation. The red solid line represents the sensitivity calculated by the above formula. The blue dashed line represents the relationship between the frequency shift and refractive index change obtained by linear fitting. From this, we can see that the relationship obtained by linear fitting is $y = 0.05x + 1.54$, $R^2 = 0.9989$. The obtained value of R^2 indicates that that the sensor has a good linearity and a good degree of fit. Therefore, the final sensitivity of the refractive index sensor is 50 GHz RIU^{-1}. Then we can calculate the sensor's LOD according to the regression equation [55, 56] LOD $= 3\alpha/S$, where α is the output uncertainty. The LOD

Figure 12. Frequency shift and sensitivity as a function of the refractive index.

is the lowest level detected with a fidelity of 99%. By considering the output uncertainty of 1%, the LOD of the sensor is 5.9×10^{-5} RIU. Table 1 shows the comparison between the structure proposed here and the previously reported device. It can be clearly seen that the absorber proposed here has a more impressive sensitivity and number of absorption peaks.

Table 1. Comparison of the proposed multi-band device with previously reported devices.

References	Operating	Number of absorption peaks	Sensitivity
[45]	0.1–2.25 THz	Five	41.9 GHz RIU^{-1} (fitting)
[57]	1.2–2.0 GHz	Two	77.25 nm RIU^{-1}
[58]	0.1–100 THz	Two	1200 nm RIU^{-1}
[59]	0.49–0.51 THz	One	23.08 GHz RIU^{-1}
[60]	1.8–2.1 THz	One	37.88 GHz RIU^{-1} (polar liquids)
Proposed	0.1–1.9 THz	Three	50 GHz RIU^{-1} (fitting) ($\sim$5753 nm RIU^{-1})

4. Conclusions

In summary, we have investigated graphene-based Si/PDMS multi-layer film structures. Four gradually decreasing absorption peaks were obtained in the range of 0–1.1 THz, with a maximum peak value near 100% and a minimum peak value exceeding 95%. A combination of an ECM and parameter inversion was used to explain the four absorption peaks. Due to the symmetry of the structural design and the locality of the graphene SPR, the absorbers were not sensitive to the polarization state and incident angle of the incident light. In addition, the resonance frequencies of the absorbers were not sensitive to the cell period and the parameter changes of the patterned graphene, which greatly increases the allowable manufacturing error. The resonance frequencies of the absorbers mainly depend on the height of the absorbers. Therefore, changing the thickness of Si and PDMS in the structures can form a three-band absorption refractive index sensor with a sensitivity of 50 GHz RIU^{-1} within 0–1.9 THz. The value of R^2 obtained by linear fitting was 0.9989, and the value of the LOD was 5.9×10^{-5} RIU. Due to the above characteristics, the proposed devices have inestimable potential in practical applications in absorbers and refractive index sensors for terahertz technology.

Data availability statement

All data that support the findings of this study are included within the article.

The data generated and/or analyzed during the current study are not publicly available for legal/ethical reasons but are available from the corresponding author upon reasonable request.

Acknowledgments

Conflict of interest

The authors declare no conflict of interest.

ORCID iDs

Jicheng Wang https://orcid.org/0000-0002-8280-7603
Zheng-Da Hu https://orcid.org/0000-0001-5655-3331

References

[1] Stewart M E, Anderton C R, Thompson L B, Maria J, Gray S K, Rogers J A and Nuzzo R G 2008 Nanostructured plasmonic sensors *Chem. Rev.* **108** 494–521
[2] Barnes W L, Dereux A and Ebbesen T W 2003 Surface plasmon subwavelength optics *Nature* **424** 824–30
[3] Zhao L, Zhang X, Wang J, Yu W H, Li J D, Su H and Shen X P 2016 A novel broadband band-pass filter based on spoof surface plasmon polaritons *Sci. Rep.* **6** 36069
[4] Ebbesen T W, Lezec H J, Ghaemi H F, Thio T and Wolff P A 1998 Wolff extraordinary optical transmission through sub-wavelength hole arrays *Nature* **391** 667–9
[5] Qin F *et al* 2016 Hybrid bilayer plasmonic metasurface efficiently manipulates visible light *Sci. Adv.* **2** e1501168
[6] Yang W H, Xiao S M, Song Q H, Liu Y L, Wu Y K, Wang S, Yu J, Han J C and Tsai D P 2020 All-dielectric metasurface for high-performance structural color *Nat. Commun.* **11** 1864
[7] Liu M Z, Fan Q B, Yu L and Xu T 2019 Polarization-independent infrared micro-lens array based on all-silicon metasurfaces *Opt. Express* **27** 10738–44
[8] Xu T, Agrawal A, Abashin M, Chau K J and Lezec H 2013 All-angle negative refraction and active flat lensing of ultraviolet light *Nature* **497** 470–4
[9] Wang Z, Yao K, Chen M, Chen H and Liu Y 2016 Manipulating Smith–Purcell emission with babinet metasurfaces *Phys. Rev. Lett.* **117** 157401
[10] Shelby R A, Smith D R and Schultz S 2001 Experimental verification of a negative index of refraction *Science* **292** 77–9
[11] Bao Z Y, Wang J C, Hu Z D, Balmakou A, Khakhomov S, Tang Y and Zhang C L 2019 Coordinated multi-band angle insensitive selection absorber based on graphene metamaterials *Opt. Express* **27** 31435–45
[12] Chen C, Wang Y Q, Jiang M W, Wang J, Guan J, Zhang B S, Wang L, Lin J and Jin P 2020 Parallel polarization illumination with a multifocal axicon metalens for improved polarization imaging *Nano Lett.* **20** 5428–34

[13] Zhou H P, Chen L, Shen F, Guo K and Guo Z Y 2019 A broadband achromatic metalens in mid-infrared region *Phys. Rev. Appl.* **11** 024046

[14] Zhang Y B, Tang T T, Girit C, Hao Z, Martin M C, Zettl A, Crommie M F, Shen Y R and Wang F 2009 Direct observation of a widely tunable bandgap in bilayer graphene *Nature* **459** 820–3

[15] Han Y, Liu Y X, Han L, Lin J and Jin P 2017 High-performance hierarchical graphene/metal-mesh film for optically transparent electromagnetic interference shielding *Carbon* **115** 34–42

[16] Luo L B, Wang K Y, Guo K, Shen F, Zhang X D, Yin Z P and Guo Z Y 2017 Tunable manipulation of terahertz wavefront based on graphene metasurfaces *J. Opt.* **19** 115104

[17] Yin Z P *et al* 2018 Tunable dual-band terahertz metalens based on stacked graphene metasurfaces *Opt. Commun.* **429** 41–5

[18] Gou K, Li Z and Guo Z Y 2020 Graphene-integrated plasmonics metasurface for active controlling artificial second harmonic generation *IEEE Access* **8** 159879

[19] Koppens F H L, Chang D E and García de Abajo F J 2011 Graphene plasmonics: a platform for strong light–matter interactions *Nano Lett.* **11** 3370–7

[20] Nikitin A Y, Guinea F, Garcia-Vidal F J and Martin-Moreno L 2011 Fields radiated by a nanoemitter in a graphene sheet *Phys. Rev.* B **84** 195446

[21] Wu C, Fang Y, Luo L, Gou K and Guo Z Y 2020 A dynamically tunable and wide-angle terahertz absorber based on graphene-dielectric grating *Mod. Phys. Lett.* B **34** 2050292

[22] Andryieuski A and Lavrinenko A V 2013 Graphene metamaterials based tunable terahertz absorber: effective surface conductivity approach *Opt. Express* **21** 9144–55

[23] Wang J C, Yang L, Hu Z D, He W J and Zheng G G 2019 Analysis of graphene-based multilayer comb-like absorption system based on multiple waveguide theory *IEEE Photonics Technol. Lett.* **31** 561–4

[24] Gou Z Y, Nie X R, Shen F, Zhou H P, Zhou Q F, Gao J and Gou K 2018 Actively tunable terahertz switches based on subwavelength graphene waveguide *Nanomaterials* **89** 665

[25] Wang X S, Xia X S, Wang J C, Zhang F, Hu Z D and Liu C 2015 Tunable plasmonically induced transparency with unsymmetrical graphene-ring resonators *J. Appl. Phys.* **118** 013101

[26] Luo L B, Wang K Y, Ge C W, Gou K, Shen F, Yin Z P and Gou Z Y 2017 Actively controllable terahertz switches with graphene-based nongroove gratings *Photon. Res.* **5** 604–11

[27] Wang J C, Wang X S, Hu Z D, Zheng G G and Zhang F 2017 Peak modulation in multi-cavity-coupled graphene-based waveguide system *Nanoscale Res. Lett.* **12** 9

[28] Wu B, Hu Y, Zhao Y T, Lu W B and Zhang W 2018 Large angle beam steering THz antenna using active frequency selective surface based on hybrid graphene-gold structure *Opt. Express* **26** 15353–61

[29] Xia X S, Wang J C, Zhang F, Hu Z D, Liu C, Yan X and Yuan L 2015 Multi-mode plasmonically induced transparency in dual coupled graphene-integrated ring resonators *Plasmonics* **10** 1409–15

[30] Liu C, Qi L and Zhang X 2018 Broadband graphene-based metamaterial absorbers *AIP Adv.* **8** 015301

[31] Yang J W, Zhu Z H, Zhang J F, Guo C C, Xu W, Liu K, Yuan X D and Qin S Q 2018 Broadband terahertz absorber based on multi-band continuous plasmon resonances in geometrically gradient dielectric-loaded graphene plasmon structure *Sci. Rep.* **8** 3239

[32] Wang J C, Yang L, Wang M, Hu Z D, Deng Q L, Nie Y G, Zhang F and Sang T 2019 Perfect absorption and strong magnetic polaritons coupling of graphene-based silicon carbide grating cavity structures *J. Phys. D: Appl. Phys.* **52** 015101

[33] Sabah C, Dincer F, Karaaslan M, Unal E, Akgol O and Demirel E 2014 Perfect metamaterial absorber with polarization and incident angle independencies based on ring and cross-wire resonators for shielding and a sensor application *Opt. Commun.* **322** 137–42

[34] Wang W, Yan F P, Tan S Y, Zhou H and Hou Y F 2017 Ultrasensitive terahertz metamaterial sensor based on vertical split ring resonators *Photon. Res.* **5** 571–7

[35] Singh R J, Cao W, Al-Naib I, Cong L Q, Withayachumnankul W and Zhang W L 2014 Ultrasensitive terahertz sensing with high-Q Fano resonances in metasurfaces *Appl. Phys. Lett.* **105** 171101

[36] Yan X *et al* 2019 The terahertz electromagnetically induced transparency-like metamaterials for sensitive biosensors in the detection of cancer cells *Biosens. Bioelectron.* **126** 485–92

[37] Chen J, Nie H, Peng C, Qi S B, Tang C J, Zhang Y, Wang L H and Park G 2018 Enhancing the magnetic plasmon resonance of three-dimensional optical metamaterials via strong coupling for high-sensitivity sensing *J. Lightwave Technol.* **36** 3481–4

[38] Wu P C, Hsu W L, Chen W T, Huang Y W, Liao C Y, Liu A Q, Zheludev N I, Sun G and Tsaia D P 2015 Plasmon coupling in vertical split-ring resonator metamolecules *Sci. Rep.* **5** 1–5

[39] Wang W, Yan F Q, Tan S Y, Li H S, Du X M, Zhang L N, Bai Z Y, Cheng D, Zhou H and Hou Y F 2019 Symmetry breaking and resonances hybridization in vertical split ring resonator metamaterials and the excellent sensing potential *J. Lightwave Technol.* **37** 5149–57

[40] Astorino M D, Fastampa R, Frezza F, Maiolo L, Marrani M, Missori M, Muzi M, Tedeschi N and Veroli A 2018 Polarization-maintaining reflection-mode THz time-domain spectroscopy of a polyimide based ultra-thin narrow-band metamaterial absorber *Sci. Rep.* **8** 1985

[41] Hu X, Xu G Q, Wen L, Wang H C, Zhao Y C, Zhang Y X, Cumming D R S and Chen Q 2016 Metamaterial absorber integrated microfluidic terahertz sensors *Laser Photon. Rev.* **10** 962–9

[42] Purkayastha A, Srivastava T and Jha R 2016 Ultrasensitive THz—plasmonics gaseous sensor using doped graphene *Sens. Actuators* B **227** 291–5

[43] Yao J, Chen Y, Ye L, Liu N, Cai G and Liu Q H 2017 Multiple resonant excitations of surface plasmons in a graphene stratified slab by Otto configuration and their independent tuning *Photon. Res.* **5** 377–84

[44] Song J C *et al* 2016 Efficient excitation of multiple plasmonic modes on three-dimensional graphene: an unexplored dimension *ACS Photon.* **3** 1986–92

[45] Islam M S *et al* 2020 Tunable localized surface plasmon graphene metasurface for multiband superabsorption and terahertz sensing *Carbon* **158** 559–67

[46] Hu J G, Qing Y M, Yang S Y, Ren Y Z, Wu X H, Gao W Q and Wu C Y 2017 Tailoring total absorption in a graphene monolayer covered subwavelength multilayer dielectric grating structure at near-infrared frequencies *J. Opt. Soc. Am. B.* **34** 861–8

[47] Zhu Z H, Guo C C, Liu K, Ye W M, Yuan X D, Yang B and Ma T 2012 Metallic nanofilm half-wave plate based on magnetic plasmon resonance *Opt. Lett.* **37** 698–700

[48] Hwang E H and Sarma S D 2007 Dielectric function screening and plasmons in two-dimensional graphene *Phys. Rev.* B **75** 205418

[49] Falkovsky L A and Pershoguba S S 2007 Optical far-infrared properties of a graphene monolayer and multilayer *Phys. Rev.* B **76** 153410

[50] Hanson G W 2008 Dyadic Green's functions and guided surface waves for a surface conductivity model of graphene *J. Appl. Phys.* **103** 064302

J. Phys. D: Appl. Phys. **54** (2021) 505306

Z Bao *et al*

[51] Iskander M F 2013 *Electromagnetic Fields and Waves* 2nd edn (Long Grove, IL: Waveland Press)

[52] Bao Z Y, Tang Y, Hu Z D, Zhang C L, Balmakou A, Khakhomov S, Semchenko I and Wang J C 2020 Inversion method characterization of graphene-based coordination absorbers incorporating periodically patterned metal ring metasurfaces *Nanomaterials* **10** 1102

[53] Smith D R, Schultz S, Markoš P and Soukoulis C M 2002 Determination of effective permittivity and permeability of metamaterials from reflection and transmission coefficients *Phys. Rev.* B **65** 195104

[54] Smith D R, Vier D C, Koschny T and Soukoulis C M 2005 Electromagnetic parameter retrieval from inhomogeneous metamaterials *Phys. Rev.* E **71** 036617

[55] Guider R, Gandolfi D, Chalyan T, Pasquardini L, Samusenko A, Pederzolli C, Pucker G and Pavesi L 2015 Sensitivity and limit of detection of biosensors based on ring resonators *Sens. Bio-Sens. Res.* **6** 99–102

[56] Homola J 2008 Surface plasmon resonance sensors for detection of chemical and biological species *Chem. Rev.* **108** 462–93

[57] Meng F, Wu Q, Erni D, Wu K and Lee J 2012 Polarization-independent metamaterial analog of electromagnetically induced transparency for a refractive-indexbased sensor *IEEE Trans. Microw. Theory Tech.* **60** 3013–22

[58] Chen C Y, Un I W, Tai N H and Yen T J 2009 Asymmetric coupling between subradiant and superradiant plasmonic resonances and its enhanced sensing performance *Opt. Express* **17** 15372–80

[59] Wang Y, Cheng W, Qin J and Han Z H 2019 Terahertz refractive index sensor based on the guided resonance in a photonic crystal slab *Opt. Commun.* **434** 163–6

[60] Chen X and Fan W 2019 Toroidal metasurfaces integrated with microfluidic for terahertz refractive index sensing *J. Phys. D: Appl. Phys.* **52** 485104